Computational Fluid Dynamics Suggests Ecological Diversification among Stem-Gnathostomes

Humberto G. Ferrón,[1,2,5,*], Carlos Martínez-Pérez,[1,2], Imran A. Rahman,[3], Víctor Selles de Lucas,[4], Héctor Botella,[2] and Philip C. J. Donoghue,[1,*]

[1]School of Earth Sciences, University of Bristol, Life Sciences Building, Tyndall Avenue, Bristol BS8 1TQ, UK.

[2]Instituto Cavanilles de Biodiversidad i Biología Evolutiva, Universitat de València, C/ Catedrático José Beltrán Martínez, 2, 46980 Paterna, Valencia, Spain.

[3]Oxford University Museum of Natural History, Parks Road, Oxford OX1 3PW, UK.

[4]School of Engineering and Computer Science, University of Hull, Cottingham Rd, Hull HU6 7RX, UK.

[5]Lead Contact

*Correspondence: humberto.ferron@bristol.ac.uk, phil.donoghue@bristol.ac.uk

SUMMARY

The evolutionary assembly of the vertebrate bodyplan has been characterised as a long-term ecological trend towards increasingly active and predatory lifestyles, culminating in jawed vertebrates which dominate modern vertebrate biodiversity [1–8]. This contrast is no more stark than between the earliest jawed vertebrates and their immediate relatives, the extinct jawless, dermal armour-encased osteostracans, which have conventionally been interpreted as benthic mud-grubbers with poor swimming capabilities, and low manoeuvrability [9–12]. Using computational fluid dynamics, we show that osteostracan headshield morphology is compatible with a diversity of hydrodynamic efficiencies including passive control of water flow around the body; these could have increased versatility for adopting diverse locomotor strategies. Hydrodynamic performance varies with morphology, proximity to the substrate and angle of attack (inclination). Morphotypes with dorsoventrally oblate headshields are hydrodynamically more efficient when swimming close to the substrate, whereas those with dorsoventrally more prolate headshields exhibit maximum hydrodynamic efficiency when swimming free from substrate effects. These results suggest different hydrofoil functions among osteostracan headshield morphologies, compatible with ecological diversification and undermining the traditional view that jawless stem-gnathostomes were ecologically constrained [9–12] with the origin of jaws as the key innovation that precipitated the ecological diversification of the group [13,14].

RESULTS

The origin of vertebrates can be characterised by increased cephalisation and a number of developmental and anatomical innovations rooted in whole genome duplication, increased

gene regulation, and the diversification of neural crest cell fates [15–17]. The ecological context to this formative evolutionary episode is envisioned as successive evolutionary grades of invertebrate chordates, jawless vertebrates and jawed vertebrates, exhibiting an overall trend towards increasingly active food acquisition that culminated in the active predatory ecology of extant gnathostomes [3,4]. In this scenario, the extinct jawless 'ostracoderms' are interpreted as cumbersome deposit feeders lacking key apomorphies of jawed vertebrates including multiple pairs of appendages and an epicercal tail, as well as jaws. This popular scenario belies the challenge of constraining the biology of ostracoderms which lack living analogues, traditionally compromising attempts to derive functional interpretations of their morphology [18]. However, the development of non-destructive tomographic methods for characterizing morphology, combined with computational engineering approaches that can be used to analyse quantitatively the functional performance of biological structures [19,20], render such macroecological and macroevolutionary hypotheses testable.

To this end, we analysed the functional morphological diversity of the Silurian–Devonian Osteostraci, the jawless sister group to all jawed vertebrates, which cover all the morphological grades exhibited by ostracoderms, including forms which entirely lack paired appendages and others that possess just a single (pectoral) pair (Figure 1a). The generic semi-circular, dorsoventrally flattened (oblate) osteostracan headshield has conventionally been interpreted as an adaptation to a sedentary benthic ecology [10,11,21–24]. However, osteostracan cranial morphology exhibits greater morphological disparity, including: morphotypes that are laterally compressed (prolate) and lack pectoral fins, interpreted as adaptations for burrowing, as well as forms with lateral and rostral expansions of the headshield, interpreted as adaptations for stabilization, enhancing lift or reducing drag

[12,23,25], deterring predators [26], housing sense organs [27], substrate anchoring [28], or specialised feeding strategies [29]. Using geometric morphometrics, we characterized quantitatively the morphological diversity of osteostracan headshields and derived an empirical morphospace that we interrogated using computational fluid dynamics (CFD) to determine how variation in morphological disparity correlates to aspects of hydrodynamic performance. CFD allowed us to simulate the interaction between flow and digital models of osteostracan morphology in three dimensions, exploring not only the impact of differences in morphology, but also the attitude of the organism with respect to flow (angle of attack) and its position relative to the substrate. We explored the fluid flow and forces generated over static models, interpreting the results exclusively in terms of morphological variation and assuming comparable modes of locomotion and post-cranial morphology for all species. The post-cranial anatomy of osteostracans is relatively conservative [18] and, hence, our morphospace analysis focussed on the headshields. In this way, we were able to test competing hypotheses of osteostracan ecology based on hydrodynamic performance criteria (such as the lift-to-drag ratio).

We characterised headshield morphology for 30 species belonging to 29 different genera and representing all major groups and the systematic breadth of osteostracans, using 123 landmarks of type I–III (Figure 1b), which were subjected to Procrustes and pairwise distance analysis prior to ordination. The ensuing phylomorphospace conveys the relationship between phylogeny and morphological variation (Figure 1c), revealing widespread convergence evidenced by many pairs of taxa that are morphologically more similar than either are to their last shared ancestor. We applied CFD to eight taxa sampled from the limits of morphospace occupation, as well as the most common morphologies (Figure 1c).

We simulated both pelagic and benthic conditions with an inlet velocity of 0.3 m s^{-1}. In the pelagic scenario, eight different angles of attack were simulated at 10º intervals between 0º and 70º. In the benthic scenario, the models were positioned at three different distances above the substrate (0.1, 0.5 and 1 body lengths) (Figure 1d). This combination of parameters covers a wide range of hypothetical modes of life, allowing us to interpret the hydrodynamic performance of osteostracan headshield under different ecological scenarios. Results of the simulations were interpreted both qualitatively, by visualizing the pressure distribution at the surface of the body, and quantitatively, by calculating drag and lift coefficients, and lift-to-drag ratios.

Sensitivity analyses demonstrate that the CFD results are independent of domain and mesh size (see Data S1 and STAR Methods section, respectively). The distributions of pressure over the body vary considerably between the pelagic and benthic simulations (Figure 2). In the pelagic simulations, the highest pressures are restricted to the front of the snout, whereas in the benthic simulations they occur along part of the ventral surface of the headshield. These differences are especially extreme in dorsoventrally compressed morphotypes, such as *Stensiopelta* (Figure 2F) and *Boreaspis* (Figure 2H).

The drag coefficient (C_D) increases with the angle of attack and proximity to the substrate (Figure 3 and Table S1), showing a positive correlation with the degree of development of headshield cornual processes, in both benthic and pelagic scenarios at low angles of attack (i.e., from 0º to 20º). Under pelagic conditions, the lift coefficient (C_L) increases approximately linearly with angle of attack from 0º to 30º (Figure 3 and Table S1), exhibiting a significant

121 correlation with headshield morphology at low angles of attack (i.e., from 0º to 20º) where
122 the highest values are attained by the morphotypes that are more triangular in outline. C_L
123 achieves its acme at 40º-50º before reaching the critical or stall angle of attack, at which point
124 C_L experiences an abrupt decrease. In the benthic scenario, C_L increases greatly for all
125 morphotypes when they are located close to the substrate, but this effect is especially
126 pronounced in taxa with oblate headshields; otherwise, there is no significant correlation with
127 headshield shape. Absolute lift force generally overcomes apparent weight for all taxa at
128 realistic angles of attack (between 10º and 30º) and cruising swimming speeds (0.30 m s^{-1}) in
129 the pelagic scenario (Table S1). Moreover, the extra lift force generated when the models are
130 located close to the substrate is enough to counteract the apparent body weight for most of
131 the species at an angle of attack of 0º. The ratio between the lift and drag coefficients (L/D)
132 is widely considered as a good proxy for hydrodynamic efficiency, and this varies substantially
133 among the different morphotypes and ecological scenarios in our study (Figure 3 and Table
134 S1). Under the pelagic scenario, the maximum L/D is attained for all morphotypes at angles
135 of attack between 20º and 30º (except for *Hoelaspis* where it is attained at 40º). Under
136 benthic conditions, peak L/D is achieved for all morphotypes when they are located at 0.1
137 body lengths above the floor. Most species with dorso-ventrally oblate headshields show the
138 highest L/D under benthic scenarios, whereas more dorso-ventrally prolate morphotypes
139 achieve peak L/D under pelagic conditions. Morphologically intermediate species do not show
140 major differences between the two scenarios and *Hoelaspis* presents the lowest L/D values in
141 all cases.
142
143 **DISCUSSION**

Our analyses indicate that osteostracans with oblate headshields were hydrodynamically more efficient (i.e., they maximized lift and minimized drag) when swimming close to the substrate, whereas prolate morphotypes exhibited maximum hydrodynamic efficiency when swimming in the water column above substrate effects. We also show that headshield morphology in several osteostracan species is compatible with passive control of hydrodynamic performance through ground effect, generating extra lift when swimming close to the substrate that overcame the apparent weight of the fish. This phenomenon is widely used by modern demersal taxa (e.g., flatfishes, skates and rays) to augment lift and counteract negative buoyancy when actively swimming near the bottom [30], occurring as a consequence of the distortion of the flow and the resulting increased pressure below the organism. Patterns of variation in surface pressure (Figure 2) and lift coefficients (Figure 3) for both pelagic and benthic scenarios are also compatible with these osteostracans benefitting from ground effect during active swimming. Some living armoured benthic fishes use similar strategies to counteract negative buoyancy, exploiting ground effect when moving close to the substrate and generating lift by increasing the angle of attack when swimming in more pelagic conditions [31]. This could also be the case for some osteostracans, especially species with oblate headshield morphologies that produce the most lift through ground effect. Oblate cambered bodies (i.e., those with flat ventral sides) might also reflect other lifestyle functions, such as benthic station-holding. On the other hand, hydrodynamic performances calculated for prolate species may reflect strictly pelagic live styles, even when swimming at comparatively low speeds and high angles of attack [32]. In this sense, there are well reported cases of pelagic living fishes, with body sizes and swimming speeds comparable to those of osteostracans, that are able to swim at high angles of attack to counteract negative buoyancy in the water column.

Our results suggest that the broad disparity and widespread convergence in headshield morphology exhibited by clades of stem-gnathostomes [18] can be explained as a consequence of their hydrodynamic and ecological disparity [12]. This interpretation relies on the assumption of a similar range of body densities for the analysed taxa. Analyses of extant species have shown that cephalofoil function can be complex, and its hydrodynamic role is controversial. In this sense, an alternative scenario of lift generation, compensating for higher density in taxa with larger bony carapaces, should be also considered. However, this view is challenged by the observation that more robust osteostracan headshield morphologies (e.g., *Stensiopelta*) do not produce greater lift than taxa with more gracile headshields (e.g., *Hemicyclaspis* or *Cephalaspis*) [33]. Thus, we provide experimental evidence compatible with both ecological diversification and exploration of complex morpho-functional hydrodynamic adaptations among jawless stem-gnathostomes. Indeed, our novel results, coupled with previous research in bioengineering [34] and functional morphology [35], further suggest that mechanisms for passively controlling flow around the body may be prevalent among these groups, where they would have conferred greater manoeuvrability and versatility than previously thought [9–12]. This calls into question the prevailing view that stem-gnathostomes were ecologically constrained prior to the emergence of jawed vertebrates and the scenario of a general trend towards increasingly active food acquisition [3,4]. In this light, the ecology of early vertebrates appears to have been more diverse and complex [36,37]. Thus, we have presented evidence of adaptations to a range of different lifestyles and ecologies evolved among jawless stem-gnathostome groups before the origin of jaws, underpinning the later exploration of novel trophic strategies and enhanced locomotory capabilities that emerged with the evolution of jaws, pelvic fins and trunk musculature

[14,38,39].

ACKNOWLEDGEMENTS

We acknowledge support from H2020 in the form of a Marie Skłodowska-Curie Research Fellowship (to HF). Additional funding was provided by Oxford University Museum of Natural History (to IAR). We thank two anonymous reviewers for providing thoughtful and valuable comments on the manuscript.

AUTHOR CONTRIBUTIONS

P.C.J.D, H.G.F and H.B. devised the project. H.G.F., I.A.R. and C.M.P. designed and performed the simulations. V.S.L. performed the 3D modelling. H.G.F and P.C.J.D wrote the manuscript with the support of the other authors.

DECLARATION OF INTERESTS

The authors declare no competing interests.

FIGURE LEGENDS

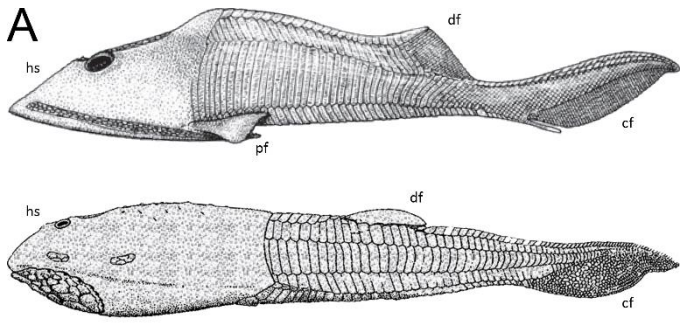
A
hs
df
pf
cf
hs
df
cf

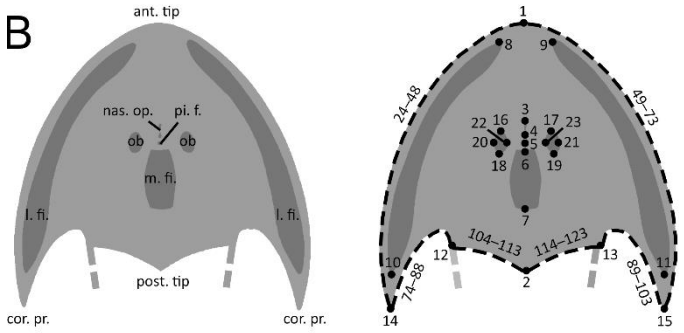
B
ant. tip
nas. op.
pi. f.
ob
ob
m. fi.
l. fi.
l. fi.
post. tip
cor. pr.
cor. pr.
1
8
9
24–48
49–73
22
16
3
17
23
20
4
5
21
18
6
19
7
104–113
114–123
10
12
13
11
74–88
2
89–103
14
15

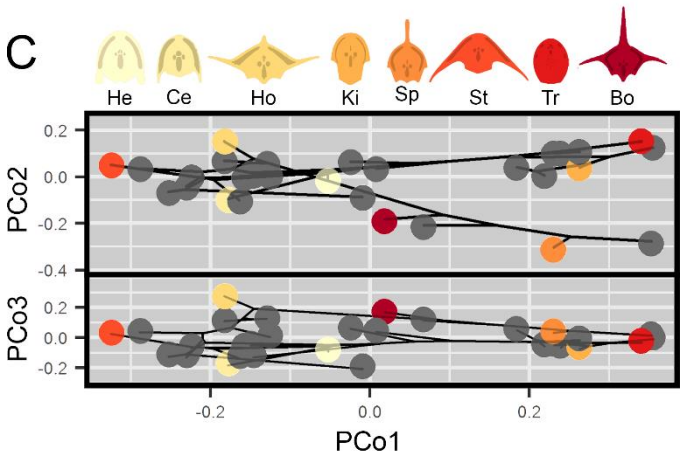
C
He
Ce
Ho
Ki
Sp
St
Tr
Bo
PCo2
0.2
0.0
-0.2
-0.4
PCo3
0.2
0.0
-0.2
-0.2
0.0
0.2
PCo1

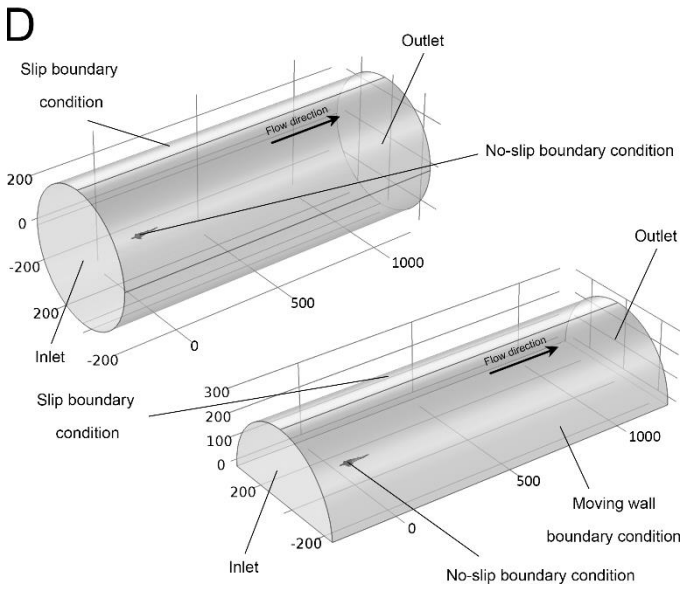
D
Outlet
Slip boundary
condition
Flow direction
No-slip boundary condition
200
0
-200
1000
500
200
Inlet
-200
0
Outlet
Slip boundary
condition
300
200
100
0
Flow direction
1000
200
500
Moving wall
boundary condition
-200
0
Inlet
No-slip boundary condition

Figure 1. Morphology of osteostracans and experimental setup. (A) General morphology of two well-known osteostracans, *Hemicyclaspis* (top) and *Trematapis* (bottom), in lateral view, indicating the position of the pectoral fins (pf), dorsal fin (df), caudal fin (cf) and headshield (hs). Modified from Janvier [18]. (B) Descriptive diagrams showing anatomical characters of the osteostracan headshield (left) and the landmark configuration used in the geometric morphometric analysis (right). Landmark 1, anterior tip of the headshield or the rostral process (ant. tip.). Landmark 2, posterior tip of the headshield (post. tip.). Landmarks 3 and 4, most anterior and most posterior medial points of the nasohypophysial opening (nas. op.) respectively. Landmark 5, pineal foramen (pi. f.). Landmarks 6 and 7, most anterior and most posterior medial points of the median field (m. fi.) respectively. Landmarks 8 and 9, most anterior points of the left and right lateral fields (l. fi.) respectively. Landmarks 10 and 11, most posterior points of the left and right lateral fields (l. fi.) respectively. Landmarks 12 and 13, left and right points of connection between the headshield and the body respectively. Landmarks 14 and 15, left and right most distal points of the corneal processes (cor. pr.) respectively. Landmarks 16–23, most anterior, posterior, lateral and medial points of the eye orbits (ob.). Landmarks 24–73, type III landmarks situated between Landmarks 1 and 14 and between Landmarks 1 and 15. Landmarks 74–103, type III landmarks situated between Landmarks 14 and 12 and between Landmarks 15 and 13. Landmarks 104–123, type III landmarks situated between Landmarks 12 and 2 and between Landmarks 13 and 2. Modified from Ferrón et al. [41]. (C) Phylomorphospace summarizing the morphological diversity of osteostracan headshields. The proportion of variance explained by PCo1–3 are 62.46%, 17.49% and 12.18% respectively. Taxa used in CFD analyses are highlighted in colour. Bo, *Boreaspis*; Ce, *Cephalaspis*; He, *Hemicyclaspis*; Ho, *Hoelaspis*; Ki, *Kiaeraspis*; Sp, *Spatulaspis*; St, *Stensiopelta*; Tr, *Trematapis*. (D) Schematic illustration of the computational domain (i.e.,

all the objects around/through which the fluid will flow) used in CFD simulations for pelagic (upper) and benthic (lower) scenarios. All measurements in mm.

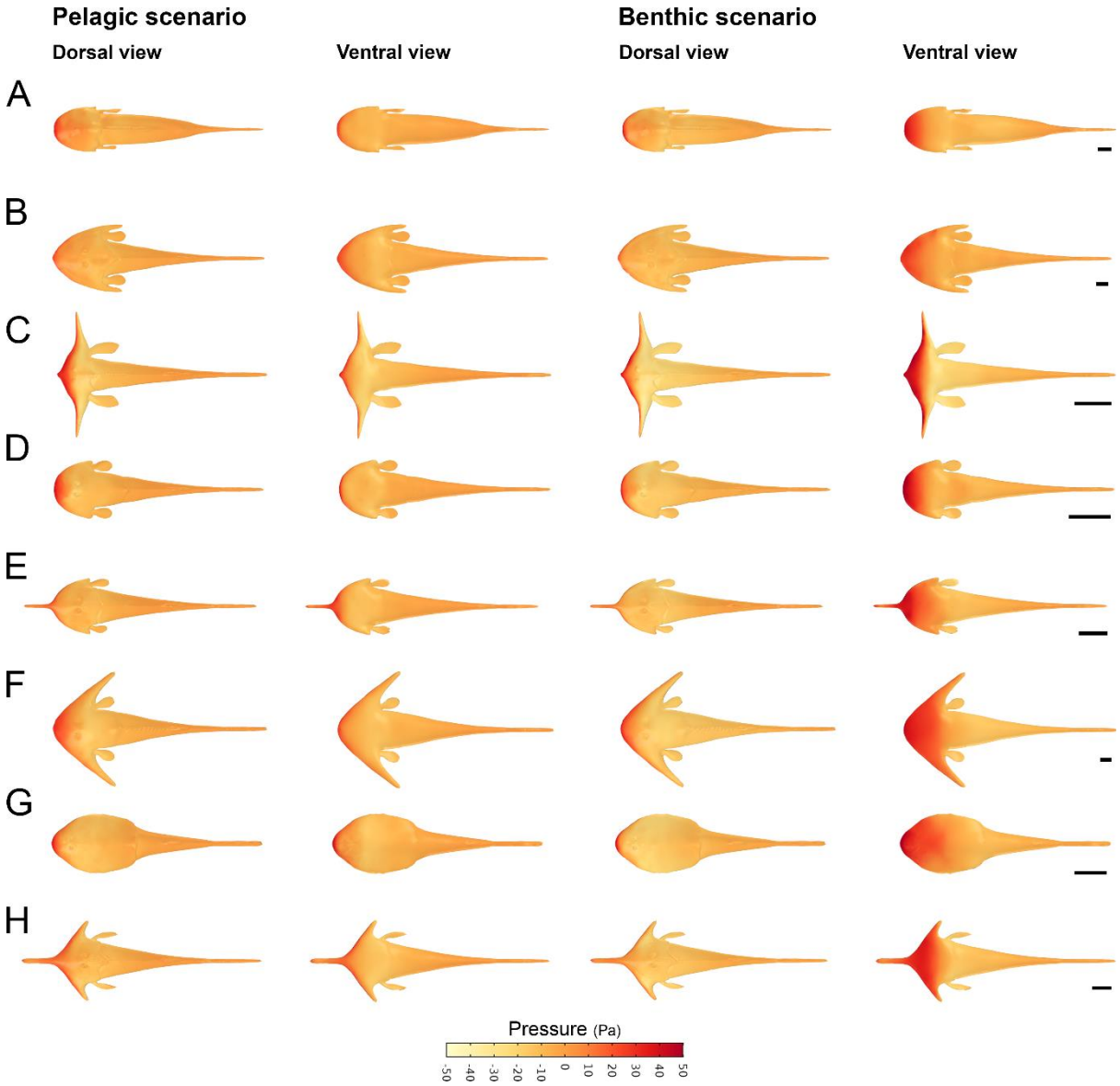

Figure 2. Results of CFD simulations showing surface pressure distributions for osteostracan models under benthic (distance above the substrate of 0.1 body lengths) and pelagic scenarios (angle of attack of 0º) with an inlet velocity of 0.3 m s^{-1}. (A) *Hemicyclaspis*. (B) *Cephalaspis*. (C) *Hoelaspis*. (D) *Kiaeraspis*. (E) *Spatulaspis*. (F) *Stensiopelta*. (G) *Tremataspis*. (H) *Boreaspis*. Note that models are lit from the top left to reveal their three-dimensional shape, but all of them display symmetrical pressure distribution patterns. Scale bar 2 cm.

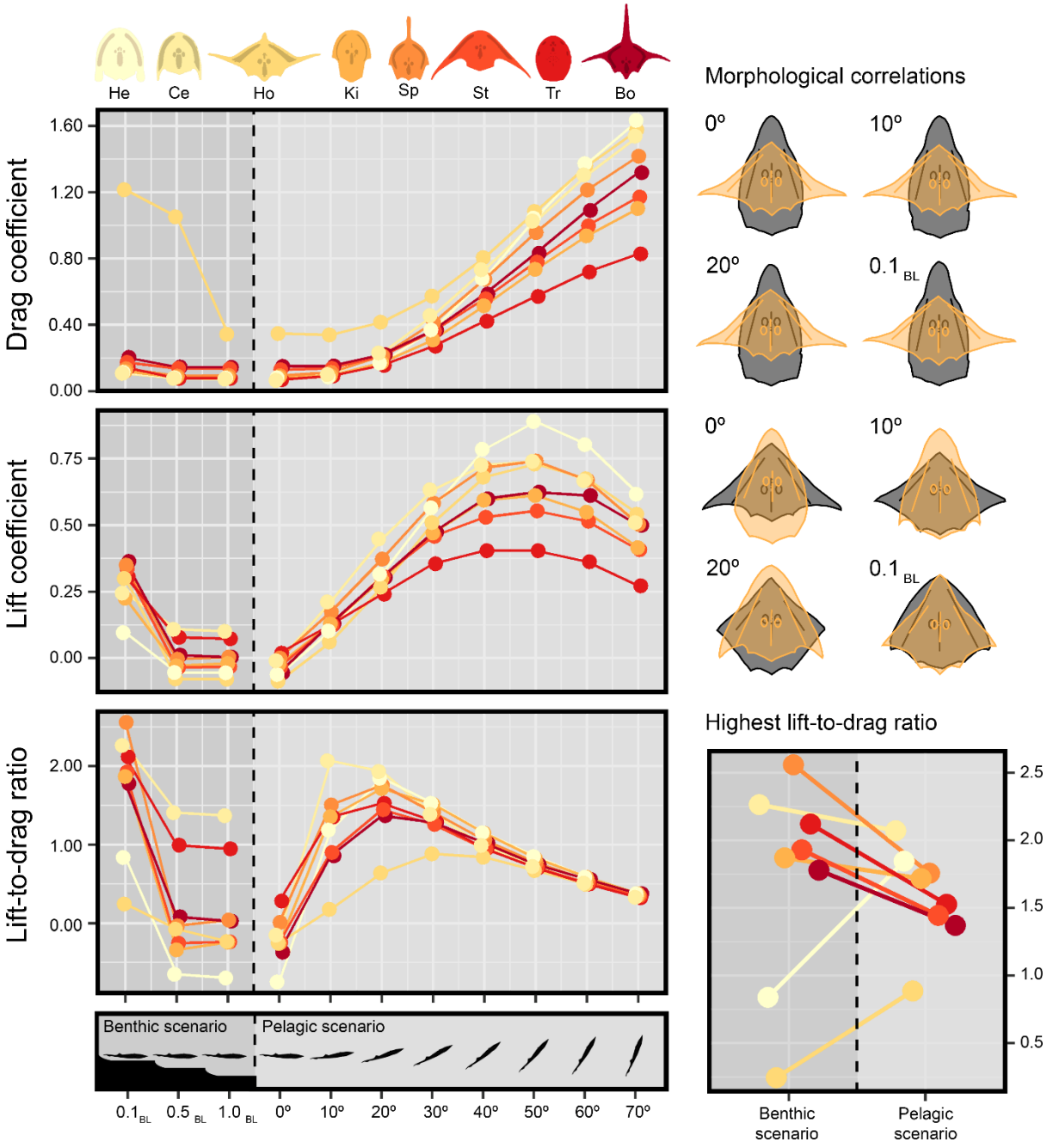

266

267 **Figure 3. Results of CFD simulations showing drag and lift coefficients and the lift-to-drag**
268 **ratio, together with associated morphological correlations, under different experimental**
269 **conditions (benthic scenario at 0.1, 0.5 and 1.0 body lengths (BL) above the substrate; and**
270 **pelagic scenario at angles of attack of 0º–70º) with an inlet velocity of 0.3 m s^{-1}.** Data
271 represented by points correspond to measured values. In the top right panel, grey and orange
272 landmark wireframe configurations represent headshield morphologies with higher and

lower force coefficients, respectively. Correlation results: C_D (0º): % predicted = 42.28, p-value = 0.0005; C_D (10º): % predicted = 42.16, p-value = 0.0001; C_D (20º): % predicted = 41.06, p-value = 0.0003; C_D (0.1_{BL}): % predicted = 34.28, p-value = 0.0077; C_L (0º): % predicted = 42.15, p-value = 0.0012; C_L (10º): % predicted = 21.07, p-value = 0.0544; C_L (20º): % predicted = 22.48, p-value = 0.0518; C_L (0.1_{BL}): % predicted = 3.01, p-value = 0.6921. Bo, *Boreaspis*; Ce, *Cephalaspis*; He, *Hemicyclaspis*; Ho, *Hoelaspis*; Ki, *Kiaeraspis*; Sp, *Spatulaspis*; St, *Stensiopelta*; Tr, *Trematapsis*. See also Table S1.

STAR METHODS

RESOURCE AVAILABILITY

Lead contact

Further information and requests for resources should be directed to and will be fulfilled by the Lead Contact, Humberto G. Ferron (Humberto.Ferron@bristol.ac.uk).

Materials Availability Statement

This study did not generate new unique reagents.

Data and code availability

The datasets generated during this study are available at the Bristol Research Data Facility (https://data.bris.ac.uk/data/dataset/1bjnv53uzx5dm2nw0q2tdtbqji).

EXPERIMENTAL MODEL AND SUBJECT DETAILS

Geometric morphometric analysis

We limited our study to species of established taxa and conducted analyses at generic level, with each genus represented by a single specimen. We used the type species and holotype specimen for each genus except where this specimen was poorly preserved; in such cases, another well-defined species was used instead. We included a total of 30 specimens in the analysis, some of which exhibited minor deformation due to dorso-ventral compression (Table S2). This deformation was not corrected for due to the difficulties in doing so without introducing additional sources of error; previous work has demonstrated that biological signal is still retained when deformation is minor [40]. Images of specimens for digitization were obtained from photographs or published reconstructions (Data S2).

METHOD DETAILS

Geometric morphometric analysis

The morphological diversity of osteostracan headshields was summarized and numerically described using geometric morphometrics, following the procedure detailed in Ferrón et al. [41]. We digitized a total of 123 landmarks of type I, II and III on selected images using TpsDig v.2.26 [42] (Figure 1b). Type III landmarks were equally interpolated along the specimen outline in six different open curves. The number of Type III landmarks chosen to represent each curve was determined visually, reflecting the complexity and relative length of each part of the headshield. Variation in translation, rotation and size from the original landmark configurations was removed by generalized Procrustes analysis (GPA) in MorphoJ v. 1.06d [43] without implementing sliding methods for Type III landmarks. This choice is fully justified as sliding and non-sliding semilandmark methods provide similar superimpositions and PCA morphospaces (Figure S1 and Table S3) [44]. Distance matrices were obtained considering Euclidean distances and subjected to principal coordinate analysis in the packages ‘cluster’

[45] and ‘ape’ [46] in R [47]. Morphospaces and phylomorphospaces were constructed using the R packages ‘Phytools’ [48] and ‘ggplot2’ [49] based on pre-ordination ancestral state estimation [50]. Ancestral state reconstruction was achieved through stochastic character state mapping [51] using the R package ‘geomorph’ [52]. This analysis was based on the phylogenetic relationships proposed by Samson [53], after modification in Mesquite [54] and time-calibration in the R package ‘paleotree’ [55], according to the stratigraphic ranges published by Samson et al [56] (Data S3).

Three-dimensional virtual modelling

Eight species of osteostracans ("*Boreaspis*" *ceratops*, *Cephalaspis lyelli*, *Hemicyclaspis murchisoni*, *Hoelaspis angulata*, *Kiaeraspis auchenaspidoides*, *Spatulaspis robusta*, *Stensiopelta pustulata* and *Trematapsis schmidti*), covering a good representation of all occupied regions of the morphospace (Figure 1c), were modelled virtually using 3D Studio Max (Data S4). Digital models obtained by three-dimensional virtual modelling have been shown to be reliable tools to assess function through computational analysis, providing very similar results to those derived from tomographic or surface-based techniques [57]. Here, modelling was based on photographs of fossil specimens and/or published reconstructions in multiple views (Table S4; see also Table S2 for a list of the specimens studied first hand). Complete headshields of all selected species are known and are usually preserved as three-dimensional structures, ensuring the accuracy of reconstructions. The postcranial region was accurately modelled for taxa in which it is known (i.e., *Cephalaspis* [58]*, Hemicyclaspis* [59] and *Trematapsis* [60]), whereas a generalized osteostracan morphology was used for the remaining species. Spinal processes were represented on the dorsal line of the *Stensiopelta* model because these structures are known to be present in other zenaspidid osteostracans

345 [18]. Pectoral fins were modelled as paddle-like structures [61,62] and were positioned
346 according to the location of the area of attachment. Digital reconstructions were scaled to life
347 size using Netfabb Basic and converted into NURBS surface using Geomagic Studio.
348
349 **Computational fluid dynamics analyses**
350 Simulations of water flow around the three-dimensional osteostracan models were
351 performed using COMSOL Multiphysics 5.2 (www.comsol.com). Two different computational
352 domains were used to emulate pelagic and benthic conditions. For the pelagic scenario, the
353 computational domain consisted of a three-dimensional cylinder (1500 mm in length and 300
354 mm in diameter) in which the osteostracan model was centrally fixed and positioned at eight
355 different angles of attack (0º to 70º, every 10º) (Figure 1d). For the benthic scenario, the
356 computational domain consisted of a three-dimensional half-cylinder (1500 mm in length and
357 300 mm in diameter) in which the osteostracan model was fixed at 0.1, 0.5 and 1.0 body
358 lengths above the lower surface of the domain (Figure 1d). We evaluated the domain size to
359 confirm it was sufficiently large that it did not influence fluid flow (Data S1).
360
361 An inlet with a normal inflow velocity boundary condition with a turbulence intensity of 0.05
362 was defined at one end of the domain, and an outlet with a zero pressure boundary condition
363 was specified at the opposing end. Boundaries at the top and sides of the domain were “open”
364 (slip boundary condition), approximating flow through the domain, whereas the boundaries
365 at the water–fossil interface were “solid” (no-slip boundary condition), fixing the fluid velocity
366 at zero. The flat lower boundary of the half-cylinder used only in the benthic scenario was
367 assigned a “moving wall” boundary condition, given the same velocity as the inlet. In all cases,
368 an automatic wall treatment was used, with surface roughness not specified. The domain was

meshed using free tetrahedral elements and the 'normal' mesh size parameter in COMSOL Multiphysics. To determine the influence of mesh size on the results of the CFD simulations, we used three different meshes in an initial exploration of mesh quality for the *Kiaeraspis* and *Stensiopelta* models, corresponding to the smallest and largest species, respectively. We evaluated 'coarser' (maximum element size of 78.0 mm and minimum element size of 24.0 mm), 'coarse' (maximum element size of 60.0 mm and minimum element size of 18.0 mm), and 'normal' (maximum element size of 40.2 mm and minimum element size of 12.0 mm) meshes. In all cases, smaller elements were used in regions close to the fossil. Drag and lift results obtained from normal and coarse meshes are very similar (see table below). As a result, we selected a 'normal' mesh for use in our study because increasing the mesh quality further would necessitate a large increase in computation time without any improvement in accuracy. An inlet velocity of 0.3 m s^{-1} was considered in all the cases.

Kiaeraspis (pelagic scenario, angle of attack 40°):

Mesh	Drag force (N)	Drag coefficient	Lift force (N)	Lift coefficient
Coarser	0.00689	0.51105	0.00758	0.56289
Coarse	0.00708	0.52508	0.00797	0.59177
Normal	0.00696	0.51669	0.00801	0.59467

Stensiopelta (pelagic scenario, angle of attack 40°):

Mesh	Drag force (N)	Drag coefficient	Lift force (N)	Lift coefficient
Coarser	0.10126	0.52276	0.09647	0.49802
Coarse	0.10719	0.55337	0.10427	0.5383
Normal	0.10808	0.55797	0.10267	0.53004

Three-dimensional, incompressible flow was simulated through the domain, with a stationary solver used to compute the steady-state flow patterns. A realistic ambient flow velocity [63]

388 of 0.30 m s^{-1} was simulated (Reynolds numbers of 17100 to 64500). The Reynolds averaged
389 Navier-Stokes (RANS) equations were solved using the shear stress transport (SST) turbulence
390 model and a segregated solver algorithm; segregated iterations terminated when the relative
391 tolerance (0.001) exceeded the relative error, computed as the minimum of the solution-
392 based error and the error given by the Residual factor (1000) times the residual-based error.
393 The effect of increasing inlet velocity was tested in parallel by simulating inlet velocities of
394 0.65 and 1.00 m s^{-1} (Reynolds numbers of 37050 to 215000; Table S1).
395
396 The results were visualized as plots of pressure (Pa) over the surface of the osteostracan
397 models. Drag and lift forces and their coefficients (C_D and C_L) were calculated to quantify the
398 flow around the digital reconstructions. For this, the headshield area was taken as the
399 reference area. Apparent weight of each taxon was also calculated for comparative purposes
400 assuming a body density of 1100 kg m^{-3} [64]. This value is in agreement with previous
401 estimations on other ostracoderms considering the distribution and density of dermal bone,
402 soft tissues and internal cavities [65]. All COMSOL Multiphysics files containing the
403 simulations are available in the Bristol Research Data Facility
404 (https://data.bris.ac.uk/data/dataset/1bjnv53uzx5dm2nw0q2tdtbqji)..
405
406 **QUANTIFICATION AND STATISTICAL ANALYSIS**
407 Phylogenetic generalized least square (PGLS) analysis was undertaken in MorphoJ v. 1.06d
408 [43] to test for correlations between shape changes and C_D and C_L. These analyses were
409 performed for one benthic (0.1_{BL}) and three pelagic (at 0º, 10º and 20º) scenarios, which were
410 considered the most biologically realistic conditions. In all cases, we considered 0.05 as the
411 level of statistical significance.

412

413 **SUPPLEMENTAL INFORMATION FILE LEGENDS**

414 **Data S1. Sensitivity analysis of domain size. Related to STAR Methods.**

415 **Data S2. Images used for the geometric morphometric analysis. Related to STAR Methods.**

416 **Data S3. R code and files used in the construction of the phylomorphospaces. Related to**

417 **STAR Methods.**

418 **Data S4. Three-dimensional models used for the computational fluid dynamics analyses.**

419 **Related to STAR Methods.**

420 **Table S1. Results of all CFD analyses performed for the eight selected species of**

421 **osteostracans including details of how the Reynolds number, apparent weight, and the drag**

422 **and lift coefficients and lift-to-drag ratios were calculated. Related to Figure 3.**

423

424 **REFERENCES**

425 1. Mallatt, J.O.N. (1984). Feeding ecology of the earliest vertebrates. Zool. J. Linn. Soc.-

426 Lond. *82*, 261–272.

427 2. Denison, R.H. (1961). Feeding mechanisms of Agnatha and early gnathostomes. Am.

428 Zool. *1*, 177–181.

429 3. Gans, C., and Northcutt, R.G. (1983). Neural crest and the origin of vertebrates: a new

430 head. Science *220*, 268–273.

431 4. Northcutt, R.G., and Gans, C. (1983). The genesis of neural crest and epidermal

432 placodes: a reinterpretation of vertebrate origins. Q. Rev. Biol. *58*, 1–28.

433 5. Gans, C. (1989). Stages in the origin of vertebrates: analysis by means of scenarios. Biol.

434 Rev. *64*, 221–268.

6. Mallatt, J. (1985). Reconstructing the life cycle and the feeding of ancestral vertebrates. In Evolutionary Biology of Primitive Fishes, R.E. Foreman, A. Gorbman, J.M. Dodd, and R. Olsson, eds. (New York and London: Plenum Press), pp. 59–68.
7. Mallatt, J. (1996). Ventilation and the origin of jawed vertebrates: a new mouth. Zool. J. Linn. Soc.-Lond. *117*, 329–404.
8. Mallatt, J. (1984). Early vertebrate evolution: pharyngeal structure and the origin of gnathostomes. J. Zool. *204*, 169–183.
9. Aleyev, Y., and Novitskaya, L.I. (1983). Experimental study of hydrodynamic qualities of Devonian heterostracans. Palaeontol. J. *1*, 3–12.
10. White, E.I., and Toombs, H.A. (1983). The cephalaspids from the Dittonian section at Cwm Mill, near Abergavenny, Gwent. Bull. Br. Mus. Nat. Hist. (Geol.) *37*, 149–171.
11. Belles-Isles, M. (1987). La nage et l'hydrodynamique de deux Agnathes du Paléozoïque: *Alaspis macrotuberculata* et *Pteraspis rostrata*. Neues. Jahrb. Geol. P.-A. *175*, 347–376.
12. Mark-Kurik, E. (1992). Functional aspects of the armour in the early vertebrates. In Fossil fishes as living animals, E. Mark-Kurik, ed. (Tallin, Estonia: Academy of Sciences of Estonia), pp. 107–115.
13. Miles, R.S. (1969). Features of Placoderm Diversification and the Evolution of the Arthrodire Feeding Mechanism. Earth Environ. Sci. Trans. R. Soc. Edinb. *68*, 123–170.
14. Anderson, P.S., Friedman, M., Brazeau, M.D., and Rayfield, E.J. (2011). Initial radiation of jaws demonstrated stability despite faunal and environmental change. Nature *476*, 206–209.
15. Marlétaz, F., Firbas, P.N., Maeso, I., Tena, J.J., Bogdanovic, O., Perry, M., Wyatt, C.D., de La Calle-Mustienes, E., Bertrand, S., and Burguera, D. (2018). *Amphioxus* functional genomics and the origins of vertebrate gene regulation. Nature *564*, 64–70.

16. Heimberg, A.M., Cowper-Sal, R., Sémon, M., Donoghue, P.C., and Peterson, K.J. (2010). microRNAs reveal the interrelationships of hagfish, lampreys, and gnathostomes and the nature of the ancestral vertebrate. Proc. Natl. Acad. Sci. U.S.A. *107*, 19379–19383.
17. Donoghue, P.C., Graham, A., and Kelsh, R.N. (2008). The origin and evolution of the neural crest. Bioessays *30*, 530–541.
18. Janvier, P. (1996). Early vertebrates (Oxford: Clarendon Press).
19. Cunningham, J.A., Rahman, I.A., Lautenschlager, S., Rayfield, E.J., and Donoghue, P.C. (2014). A virtual world of paleontology. Trends in ecology & evolution *29*, 347–357.
20. Rahman, I.A. (2017). Computational fluid dynamics as a tool for testing functional and ecological hypotheses in fossil taxa. Palaeontology *60*, 451–459.
21. Bunker, S.J., and Machin, K.E. (1991). The hydrodynamics of cephalaspids. In Biomechanics in evolution, J.M.V. Rayner, and R.J. Wootton, eds. (Cambridge and New York: Cambridge University Press), pp. 113–129.
22. Janvier, P., and Lawson, J.D. (1985). Environmental framework of the diversification of the Osteostraci during the Silurian and Devonian. Philos. Trans. R. Soc. B *309*, 259–272.
23. Afanassieva, O.B. (1992). Some peculiarities of osteostracan ecology. In Fossil fishes as living animals, E. Mark-Kurik, ed. (Tallin, Estonia: Academy of Sciences of Estonia), pp. 61–70.
24. Morrissey, L.B., Braddy, S.J., Bennett, J.P., Marriott, S.B., and Tarrant, P.R. (2004). Fish trails from the lower old red sandstone of Tredomen Quarry, Powys, southeast Wales. Geol. J. *39*, 337–358.
25. Dec, M. (2019). Hydrodynamic performance of psammosteids: New insights from computational fluid dynamics simulations. Acta Palaeontol. Pol. *64*, 679–684.

26. Janvier, P. (1997). Contribution à la connaissance de l'anatomie et de la systématique du genre *Boreaspis* Stensiö (Agnatha, Cephalaspidomorphi, Osteostraci), du Dévonien inférieur du Spitsberg. Ann. Paleontol. *63*, 1–32.
27. Voichyshyn, V. (2006). New osteostracans from the Lower Devonian terrigenous deposits of Podolia, Ukraine. Acta Palaeontol. Pol. *51*, 131–142.
28. Janvier, P. (1985). Les Céphalaspides du Spitsberg. Anatomie, phylogénie et systématique des Ostéostracés siluro-dévoniens. Révision des Ostéostracés de la formation de Wood Bay (Dévonien inférieur du Spitsberg) (Paris: CNRS édition).
29. Dineley, D.L. (1994). Cephalaspids from the Lower Devonian of Prince of Wales Island, Canada. Palaeontology *37*, 61–70.
30. Vogel, S. (1994). Life in moving fluids: the physical biology of flow (Princeton: Princeton University Press).
31. Nowroozi, B.N., Strother, J.A., Horton, J.M., Summers, A.P., and Brainerd, E.L. (2009). Whole-body lift and ground effect during pectoral fin locomotion in the northern spearnose poacher (*Agonopsis vulsa*). Zoology *112*, 393–402.
32. He, P., and Wardle, N.C. (1986). Tilting behaviour of the Atlantic mackerel, *Scomber scombrus*, at low swimming speeds. Journal of Fish Biology *29*, 223–232.
33. Afanassieva, O.B. (2018). Morphogenetic Features of the Exoskeleton in Early Jawless Vertebrates (Osteostraci, Agnatha): Geometry of the Shield Sections. Paleontol. J. *52*, 1756–1763.
34. Botella, H., and Fariña, R.A. (2008). Flow pattern around the rigid cephalic shield of the Devonian agnathan *Errivaspis waynensis* (Pteraspidiformes: Heterostraci). Palaeontology *51*, 1141–1150.

35. Ferrón, H.G., and Botella, H. (2017). Squamation and ecology of thelodonts. PloS one *12*, e0172781.
36. Purnell, M.A. (2001). Scenarios, selection, and the ecology of early vertebrates. In Major events in early vertebrate evolution, P.E. Ahlberg, ed. (London and New York: Taylor & Francis), pp. 188–208.
37. Purnell, M.A. (2002). Feeding in extinct jawless heterostracan fishes and testing scenarios of early vertebrate evolution. Proc. R. Soc. B *269*, 83–88.
38. Anderson, P.S. (2008). Shape variation between arthrodire morphotypes indicates possible feeding niches. J. Vertebr. Paleontol. *28*, 961–969.
39. Hill, J.J., Puttick, M.N., Stubbs, T.L., Rayfield, E.J., and Donoghue, P.C. (2018). Evolution of jaw disparity in fishes. Palaeontology *61*, 847–854.
40. Angielczyk, K.D., and Sheets, H.D. (2007). Investigation of simulated tectonic deformation in fossils using geometric morphometrics. Paleobiology *33*, 125–148.
41. Ferrón, H.G., Greenwood, J.M., Martínez-Pérez, C., Botella, H., Sansom, R.S., Deline, B., and Donoghue, P.C.J. (in press.). Categorical versus geometric morphometric approaches to characterising the evolution of morphological disparity in Osteostraci (Vertebrata, stem-Gnathostomata). Palaeontology.
42. Rohlf, J. (2016). tpsDig2. v 2.26. Stony Brook University, New York.
43. Klingenberg, C.P. (2011). MorphoJ: an integrated software package for geometric morphometrics. Mol. Ecol. Resour. *11*, 353–357.
44. Esteban-Trivigno, S.D. (2011). Ecomorfología de xenartros extintos: análisis de la mandíbula con métodos de morfometría geométrica. Ameghiniana *48*, 381–398.
45. Maechler, M., Rousseeuw, P., Struyf, A., Hubert, M., and Hornik, K. (2019). cluster: Cluster Analysis Basics and Extensions. R package version 2.1.0.

46. Paradis, E., and Schliep, K. (2018). ape 5.0: an environment for modern phylogenetics and evolutionary analyses in R. Bioinformatics *35*, 526–528.
47. R Development Core Team (2017). R: A language and environment for statistical computing. R Foundation for Statistical Computing, Vienna, Austria. 2016.
48. Revell, L.J. (2012). phytools: an R package for phylogenetic comparative biology (and other things). Methods Ecol. Evol. *3*, 217–223.
49. Wickham, H. (2016). ggplot2: elegant graphics for data analysis (Springer).
50. Lloyd, G.T. (2018). Journeys through discrete-character morphospace: synthesizing phylogeny, tempo, and disparity. Palaeontology *61*, 637–645.
51. Huelsenbeck, J.P., Nielsen, R., and Bollback, J.P. (2003). Stochastic mapping of morphological characters. Syst. Biol. *52*, 131–158.
52. Adams, D.C., Collyer, M., Kaliontzopoulou, A., and Sherratt, E. (2019). Geomorph: Software for geometric morphometric analyses. R package version 3.1.0.
53. Sansom, R.S. (2009). Phylogeny, classification and character polarity of the Osteostraci (Vertebrata). J. Syst. Palaeontol. *7*, 95–115.
54. Maddison, W.P., and Maddison, D.R. (2017). Mesquite: a modular system for evolutionary analysis. Version 3.2. http://mesquiteproject.org.
55. Bapst, D.W. (2012). paleotree: an R package for paleontological and phylogenetic analyses of evolution. Methods Ecol. Evol. *3*, 803–807.
56. Sansom, R.S., Randle, E., and Donoghue, P.C. (2015). Discriminating signal from noise in the fossil record of early vertebrates reveals cryptic evolutionary history. Proc. R. Soc. B *282*, 20142245.
57. Rahman, I.A., and Lautenschlager, S. (2016). Applications of three-dimensional box modeling to paleontological functional analysis. Pal. Soc. Pap. *22*, 119–132.

58. White, E.I. (1958). On *Cephalaspis lyelli* Agassiz. Palaeontology *1*, 99–105.

59. Stensiö, E.A. (1932). The Cephalaspids of Great Britain (London: British museum, Natural History).

60. Janvier, P. (1985). Les Thyestidiens (Osteostraci) du Silurien de Saaremaa (Estonie). Première partie: Morphologie et anatomie. Ann. Paleontol. *71*, 83–147.

61. Janvier, P. (1978). Les nageoires paires des Ostéostracés et la position systématique des Céphalaspidomorphes. Ann. Paleontol. *64*, 113–142.

62. Janvier, P., Arsenault, M., and Desbiens, S. (2004). Calcified cartilage in the paired fins of the osteostracan *Escuminaspis laticeps* (Traquair 1880), from the Late Devonian of Miguasha (Québec, Canada), with a consideration of the early evolution of the pectoral fin endoskeleton in vertebrates. J. Vert. Paleontol. *24*, 773–779.

63. Videler, J.J. (2012). Fish swimming (Salisbury, United Kingdom: Springer Science & Business Media).

64. Lowndes, A.G. (1955). Density of fishes: some notes on the swimming of fish to be correlated with density, sinking factor and load carried. J. Nat. Hist. *8*, 241–256.

65. Botella, H. (2005). Microictiolitos del Devónico Inferior de Nigüella (Cordillera Ibérica); consideraciones paleobiológicas e hidrodinámicas de condrictios y agnatos primitivos. (Valencia: Universitat de Valencia).